Quantum-Limited Atomic Receiver in the Electrically Small Regime

Kevin C. Cox,[1] David H. Meyer,[1,2] Fredrik K. Fatemi,[1] and Paul D. Kunz[1]
[1]U.S. Army Research Laboratory, Adelphi, Maryland 20783, USA
[2]Department of Physics, University of Maryland, College Park, Maryland 20742, USA

(Received 19 June 2018; published 11 September 2018)

We use a quantum sensor based on thermal Rydberg atoms to receive data encoded in electromagnetic fields in the extreme electrically small regime, with a sensing volume over 10^7 times smaller than the cube of the electric field wavelength. We introduce the standard quantum limit for data capacity, and experimentally observe quantum-limited data reception for bandwidths from 10 kHz up to 30 MHz. In doing this, we provide a useful alternative to classical communication antennas, which become increasingly ineffective when the size of the antenna is significantly smaller than the wavelength of the electromagnetic field.

DOI: 10.1103/PhysRevLett.121.110502

Antennas do not obey Moore's law. As cutting-edge devices become smaller and smaller, the communication transmitter and receiver antennas present significant size constraints [1,2]. This is because fundamental principles limit the performance of a traditional antenna that is significantly smaller than the wavelength of the electromagnetic (EM) field being detected, λ. Specifically, a lossless, resonant, electrically small antenna of characteristic radius a is guaranteed to have a quality factor Q greater than the Chu limit, $Q_{\mathrm{Chu}} = \lambda^3/(2\pi a)^3$, that limits the operation bandwidth to $\mathrm{BW}_{\mathrm{Chu}} \lesssim f_0/Q_{\mathrm{Chu}}$ for carrier frequency f_0.

This limit, pioneered by Chu, Wheeler, Harrington, McLean, and others, influences the design of a wide range of communication technologies using carrier frequencies ranging from dc up to GHz frequencies [2–6]. Discovery of modest optimizations within the Chu limit constraint is still an active area of research [7,8], as well as exploration into alternative communications technologies (e.g., based on acoustics or active circuits) that are not subject to the Chu limit [9,10]. Here we introduce another alternative path: using a quantum sensor operating at the standard quantum limit (SQL) to receive classical communications.

In this Letter, we first introduce the SQL for data capacity (or channel capacity) C_{SQL} of a receiver based on a quantum sensor and perform a basic comparison with the Chu limit. For our experimental parameters, the quantum system nominally gives improvements of over 4 orders of magnitude over the Chu limit. Second, we experimentally demonstrate quantum-limited reception of signals using thermal Rydberg atoms. By achieving photon-shot-noise-limited readout and increasing the operation bandwidth beyond the decoherence rate, we observe a transition from the steady-state (SS) electromagnetically induced transparency (EIT) regime to quantum-limited scaling corresponding to operation at the SQL for 60 effective atoms [11].

A number of recent experiments have used thermal Rydberg atoms for state-of-the-art sensors of electric fields [12–19]. Most of these experiments were primarily focused on sensitivity and operated at bandwidths lower than the decoherence rates set by EIT power broadening, transit broadening, and Doppler broadening, precluding operation at the SQL. We highlight that for communication purposes, on the other hand, high bandwidth is often the goal, and the fundamental quantum limit can be reached. Our group and others have recently introduced radio-frequency (rf) communications receivers using atomic sensors [20–23], but have not explicitly reached the SQL. Previous receivers based on Rydberg atoms [20–22] were also not deeply in the electrically small regime, where significant advantages over traditional receiver antennas are apparent.

Atomic sensors are not antennas, at least in the traditional sense. Traditional antennas are passive devices designed to efficiently convert free-space EM waves into signals on a transmission line. On the other hand, atomic electric field sensors often do not absorb net energy from the field, but rather use the atoms and additional laser beams to perform nondestructive sensing [24]. This sensing regime breaks a key assumption behind the Chu limit—namely, that of passive, destructive sensing—allowing a quantum sensor using a single atom to operate at an arbitrarily high bandwidth.

Consider the case where the goal of classical communication is to detect a high rate of data, given by data capacity C measured in bits per second, encoded here in the amplitude modulation of an electric field with a carrier frequency f_0. The achievable C is given by the Shannon-Hartley theorem [25], $C = f_d \log_2(1 + \mathrm{SNR}^2)$, where f_d is the rate that data symbols are sent, and SNR is the signal-to-noise ratio, in standard deviation, for detecting the electric field in a measurement window of length $t_d = 1/f_d$.

Any quantum sensor based on two-level systems observes the applied EM field as an evolution of a quantum

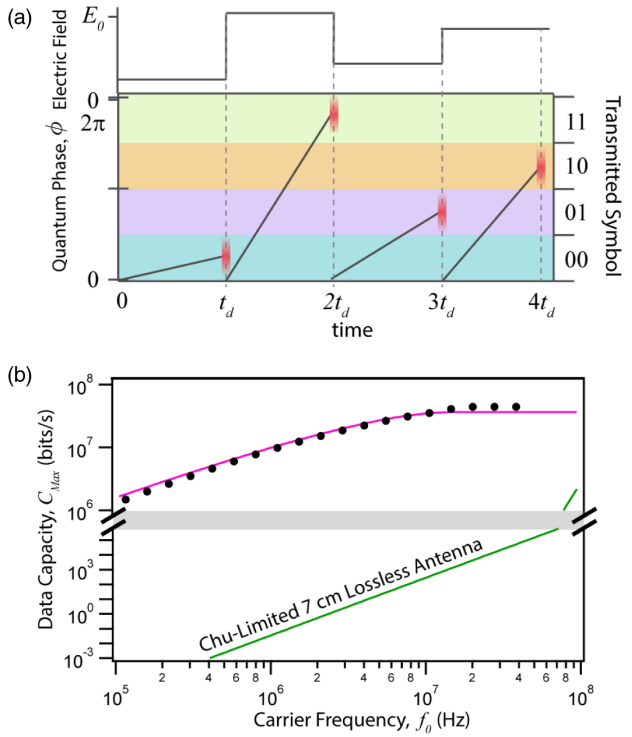

FIG. 1. The quantum limit for data capacity. (a) Data can be sent, for example, by encoding information in the strength of the electric field. The quantum sensor detects symbols by measuring the evolved phase ϕ at the end of each period, therefore inferring the transmitted symbol (right axis). (b) The Chu limit to data capacity for an efficient 7 cm classical antenna is shown in green (see text for details). The maximum standard quantum limit $C_{\max}$ for our experimental parameters is shown in pink. The corresponding maximum measured data capacity of our sensor is shown as black points.

phase ϕ characterizing a superposition state $|\psi\rangle = (1/\sqrt{2})(|g\rangle + e^{i\phi}|e\rangle)$ with quantum states $|g\rangle$ and $|e\rangle$. In the case of low-frequency sensing, exclusively studied here, an applied electric field E changes the atomic transition frequency by an amount $\delta\omega = \frac{1}{2}\alpha E^2/\hbar$. In a sensing time t_d, $\delta\omega$ accumulates into the evolved quantum phase $\phi = \delta\omega t_d$. When operating with N independent atoms, the individual collapse of atomic wave functions into either $|e\rangle$ or $|g\rangle$ limits the resolution (given by standard deviation, denoted by Δ) of a measurement of ϕ to the SQL, $\Delta\phi_{\mathrm{SQL}} = 1/\sqrt{N}$.

Figure 1(a) shows how the SQL limits communication. For communication, the continuous observable ϕ can be broken into a number of discrete binary symbols (e.g., 2 bits, 00 to 11, delineated by color in the figure). The symbols may be transmitted, as is done here, by changing the amplitude of a static or oscillatory electric field with nominal amplitude E_0. Symbols are received at bandwidth f_d by allowing ϕ to linearly evolve into a specific binary state in time t_d. In the optimum case, readout is much faster than t_d, and quantum noise is observed as an instantaneous uncertainty to each readout of ϕ [shown as red uncertainty distributions in Fig. 1(a)].

Combining the Shannon-Hartley theorem and the SQL, we derive the quantum-limited data capacity, for N independent atoms, to be

$$C_{\mathrm{SQL}} = f_d \log_2\left(1 + \frac{\delta\omega^2 N}{f_d^2}\right). \tag{1}$$

C_{SQL} increases with f_d until the argument inside the logarithm becomes approximately 4.92. This occurs at an optimal (denoted by a star) data transmission rate $f_d^* = 0.505(\delta\omega\sqrt{N})$. The corresponding optimal quantum-limited data capacity is $C_{\mathrm{SQL}}^* = 1.16(\delta\omega\sqrt{N})$. To achieve a larger SNR or data capacity, one must increase the atom number or probe an atomic state with a larger polarizability. One potential avenue is to use Rydberg states with higher principle quantum number n, where the polarizability nominally scales as n^7 [26].

In Fig. 1(b), we present a basic comparison between C_{SQL} and the classical data capacity bound arising from the Chu limit. To determine the Chu-limited data capacity, one needs to know both the bandwidth and the SNR of the classical antenna. Here we consider an efficient classical antenna with maximum Chu-limited data rate $f_d \sim \mathrm{BW}_{\mathrm{Chu}}$, whose enclosing sphere [3] has the same radius a as that required for our Rb vapor cell ($a = 3.75$ cm). We consider the classical antenna to be subjected to 50 Ω Johnson noise at room temperature, and plot for our experimental electric field 0.8 V/cm.

The maximum achievable quantum-limited data capacity of our system $C_{\max}$ is plotted versus carrier frequency f_0 as a pink line in Fig. 1(b). To obtain $C_{\max}$, we choose the optimum data rate to maximize Eq. (1) at each f_0, while enforcing $f_d <= f_0$. At $f_0 = 10^7$ Hz, we reach the optimum data rate $f_d = f_0 = f_d^*$. Subsequent increases in f_d only reduce C_{SQL}, and therefore $C_{\max}$ becomes flat (equal to C_{SQL}^*). The experimentally measured maximum capacity is shown in black points [27]. The measurements used to obtain these data are described in detail in later sections and Fig. 3(b).

The quantum sensor outperforms the efficient electrically small antenna by a factor of more than 10^4 at 10 MHz, and the advantage is even more extreme at lower frequencies. For the $a = 3.75$ cm antenna considered here, the Chu limit and SQL cross at $f_0 \approx 1.5 \times 10^8$ Hz, as the traditional antenna leaves the extreme electrically small regime. To be clear, there are other methods that surpass the nominal Chu-limited data capacity, such as using inefficient designs [28], active non-Foster circuit elements [10,29], or non-impedance-matched antennas (viable when the field wavelength is long and reflections can be tolerated). It is also important to note that for many communications applications, external noise sources—blackbody, cosmic, man-made, and atmospheric

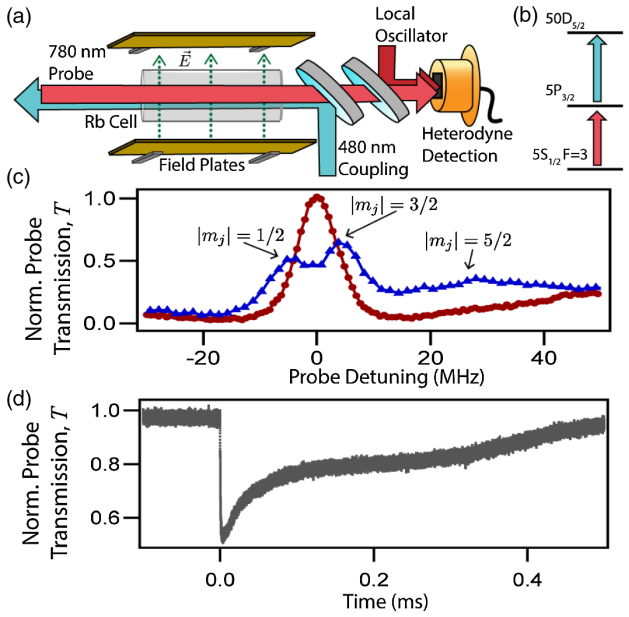

FIG. 2. (a) Experimental setup and (b) Level diagram. (c) When no E field is applied, we observe a single EIT transmission window (red circles). Low-frequency electric fields cause scalar and tensor Stark shifts that split the resonance into three peaks (blue triangles). (d) At $t = 0$, we apply a square pulse to the electric field. The probe transmission rapidly follows the applied field, but then slowly relaxes over 0.5 ms due to free charges in the glass cell that shield the electric field.

noise—can dominate the internal receiver noise, be it quantum or classical. Despite these details that require further exploration, we expect quantum sensors can provide significant benefits in sensitivity and bandwidth for certain applications.

A simplified version of our experimental setup and level diagram is shown in Figs. 2(a) and 2(b). Using two parallel plates separated by 60 mm, we apply a transverse low-frequency electric field. The 480 nm (blue) beam (tuned to the ^{85}Rb $|5P_{3/2}, F = 4\rangle$ to $|50D_{5/2}\rangle$ transition) and the 780 nm (red) beam (tuned to the $|5S_{1/2}, F = 3\rangle$ to $|5P_{3/2}, F = 4\rangle$ transition) counterpropagate to establish nearly Doppler-free EIT. In the regime of low-frequency E fields, we detect the Stark shift of the Rydberg state, $\delta\omega = \frac{1}{2}\alpha E^2$, where α is the scalar polarizability of the atomic transition, approximately constant for the low frequencies applied here. The $|50D_{5/2}\rangle$ Rydberg state splits into three sublevels due to the tensor component of the polarizability: $|m_j| = 1/2$, $|m_j| = 3/2$, $|m_j| = 5/2$. We calculate the polarizabilities of these states to be $\alpha = 2\pi(-36, 42, 212)$ MHz/(V/cm)^2, respectively [30]. In Fig. 2(c), we show a plot of the EIT transmission profile with no electric field (red circles), and with an electric field of 0.4 V/cm applied (blue triangles). The peak splits into the three m_j sublevels. To detect electric fields, we observe the change in transmission of the 780 nm probe laser through the cell as the EIT resonance frequencies are changed due to the applied electric field. For high SNR readout, we overlap the 780 nm probe beam with a strong heterodyne local oscillator detuned by 78.5 MHz. In contrast to rf systems, optical heterodyne detection allows readout with zero thermal noise; here we observe quantum shot noise to be 6 dB greater than detector noise. More details about the experimental setup can be found in our previous work [20].

An example trace is shown in Fig. 2(d). At $t = 0$ s, we turn on the electric field from zero (on EIT resonance) to 0.8 V/cm. The probe transmission (gray line), normalized to the total transmission associated with EIT, drops accordingly, corresponding to the Rydberg state shifting off of two-photon resonance. Over 0.5 ms, however, the transmitted signal relaxes to the original value, indicating a relaxation to zero of the electric field observed by the atoms. This effect has been studied in other vapor-cell-based systems and can be attributed to free charges in the glass cell shielding the electric field [12,31]. However, for reasonably high bandwidths of 100 kHz or more, we observe this relaxation effect to be less significant.

To calculate the data capacity of our receiver, we measure the SNR for detecting a quantum phase ϕ as a function of data rate f_d. Instead of explicitly operating at many different frequencies, we apply a step function in the electric field, as is done in Fig. 2(d) or the inset of Fig. 3(a), and measure the SNR of detecting the step as a function of measurement bandwidth. Specifically, for each applied step in the field, we average the probe transmission signal in a time window of length t_d [pink window in inset of Fig. 3(a)] placed adjacent to the step. The outcome of this average can be used to determine a sent data symbol [20,32]. To change the effective bandwidth, we change the length of the averaging window $t_d = 1/f_d$. We determine the SNR from the outcome of 100 independent measurements of the electric field. The resulting SNR for detecting an electric field as a function of data rate is shown as black solid data points in Fig. 3(a). By independently calibrating the photon shot noise (PSN) level, we measure and subtract out additional $1/f$ laser noise that contributes at low frequencies [plotted as open circles in Fig. 3(a)]. For simplicity we have chosen the electric field strength to create Stark shifts on the order of the EIT linewidth. However, using active stabilization of the probe laser to the EIT feature, the dynamic range can be made much larger than the linewidth. For strong fields, Rydberg state mixing must be accounted for [12].

In many quantum sensors, state selective readout means PSN is uncorrelated with atomic shot noise [33]. In EIT, on the other hand, scattering of a photon has a one-to-one correspondence with atom wave function collapse. Explicitly, the SNR that we observe is determined by the number of atoms that collapse into the EIT bright state, absorbing and scattering photons out of the probe beam during the communication time t_d. This leads to a quantum-limited SNR, $\mathrm{SNR}_{\mathrm{SQL}} = \delta\omega_{\mathrm{eff}} t_d \sqrt{QN}$, where N is the total

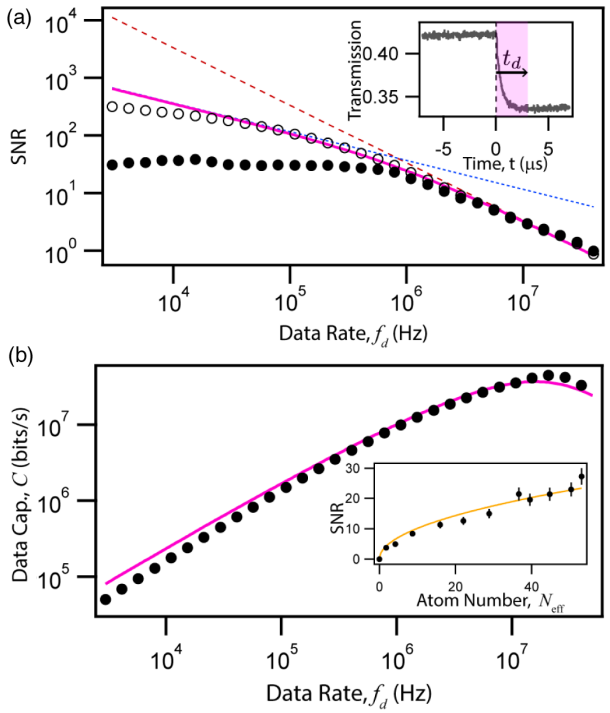

FIG. 3. Quantum-limited operation. (a) We measure probe transmission through the cell in bandwidth $f_d = 1/t_d$ by averaging for time t_d (inset). Directly measured SNR (black points) and SNR with technical noise subtracted (open circles) are plotted versus f_d. At high frequencies, we observe the standard-quantum-limited SNR scaling (red dashed line). At lower frequencies, we observe a steady-state, square-root scaling of SNR (blue dots). The data are fit to the complete quantum noise model (pink line). The SNR data (open circles) lie within 2 standard deviations of the fit over the fitted range of $f_d = 5 \times 10^4$ Hz to $f_d = 10^7$ Hz. The larger deviations at low frequencies are due to the cell shielding effect. (b) The SNR data from (a) are used to plot data capacity versus f_d. The quantum limit, for our fitted effective atom number and signal size, is shown as a pink line. Inset: We plot the SNR for receiving symbols in a bandwidth $f_d =$ 0.5 MHz as a function of the effective atom number. The data are fit to a square-root scaling.

atom number and Q is the total intrinsic quantum efficiency that includes path losses, technical noise that partially hides quantum fluctuations, noninfinite optical depth, as well as the fundamental 50% efficiency of heterodyne detection. Q can also be absorbed into an effective atom number $N_{\mathrm{eff}} = QN$, for which we observe quantum-limited operation. We also define the effective Stark shift $\delta\omega_{\mathrm{eff}}$ that accounts for reductions in the signal due to additional decoherence, nonoptimal probing, and shielding effects (with associated signal efficiency Q_{sig}), $\delta\omega_{\mathrm{eff}} = \delta\omega Q_{\mathrm{sig}}$.

If the symbol period t_d is longer than the coherence time of the dark state in the presence of the electric field, an atom is likely to scatter many times during a single symbol. In this steady-state regime, the SNR is $\mathrm{SNR_{SS}} = \sqrt{N_{\mathrm{eff}} t_d/\tau}$, where τ is the characteristic time for an atom to transition from the dark state to the bright state and scatter a photon. In Fig. 3(a), $\mathrm{SNR_{SS}}$ is displayed as a blue dotted line. If $t_d < \tau$, atoms collapse, on average, less than once in the symbol period. In this regime, the SNR can approach the quantum limit. $\mathrm{SNR_{SQL}}$ is plotted as a red dashed line in Fig. 3(a).

We fit our observed SNR in Fig. 3 to a model combining the two SNR limits, $\mathrm{SNR_{SQL}}$ and $\mathrm{SNR_{SS}}$. Since the applied Stark shift is larger than the rubidium $D2$ excited state lifetime ($\Gamma = 2\pi \times 6$ MHz), we set the scattering rate $1/\tau$ in the model to be the upper bound, $\Gamma/2$ [20]. We allow $\delta\omega_{\mathrm{eff}}$ and N_{eff} to be fit parameters. The fit is plotted as a pink line in Fig. 3(a). The fit returns $\delta\omega_{\mathrm{eff}} = 680(60)$ kHz and $N_{\mathrm{eff}} = 63(7)$. From this we deduce $Q_{\mathrm{sig}} \approx 3\%$. Further, the measured optical depth and EIT contrast allows us to approximate the total number of atoms participating in EIT to be of order 10^4, which gives the total quantum efficiency Q of approximately 0.5%. These returned values are in rough agreement with what we predict from known inefficiencies. We explicitly observe the transition from the steady-state PSN regime to the SQL regime at 800 kHz, a frequency governed by τ. Previous Rydberg electrometry experiments have focused on lower bandwidth sensing, and have not explicitly reached the regime of SQL scaling [14]. However, we emphasize that atomic wave function collapse, resulting in quantum noise in the transmitted light, limits the SNR at all bandwidths, even in the steady-state regime.

In Fig. 3(b) (inset), we plot the SNR for detecting a symbol in a bandwidth $f_d = 0.5$ MHz as a function of the effective atom number N_{eff}. Here we adjust N_{eff} by changing a static electric field, moving the EIT two-photon transition off of resonance. Figure 3(b) shows that the SNR, limited by atomic wave function collapse manifesting as PSN, indeed scales as $\sqrt{N_{\mathrm{eff}}}$ (fit displayed as solid orange line). This scaling is observed in both the steady-state and SQL-scaling regimes and can be equivalently viewed as either a consequence of atomic wave function collapse or photon shot noise.

In Fig. 3(b), we plot (black points) the data capacity C, with no noise subtractions, inferred from the measured SNR and data rate of Fig. 3(a) using the Shannon-Hartley theorem. C_{SQL}, using $\delta\omega_{\mathrm{eff}}$ and N_{eff}, is shown as a pink line. These data and theory are the same as that of Fig. 1(b) except plotted directly versus f_d, leading to a drop in C when $f_d > f_d^* = 3 \times 10^7$ Hz. At the optimum data rate we achieve $C^*_{\mathrm{SQL}} = 4 \times 10^7$ bits/s. We highlight that further improvements can only be realized by increasing the effective atom number, the effective polarizability, or by adding entanglement between the atoms.

More broadly, Fig. 3 associates the performance of our atomic sensor used for classical data reception to the foundational quantum principles governing the system. This is important, for one, because it sets a fundamental bound—much like the Chu limit for traditional antennas—on the system's capabilities based on the basic resources

used. Second, the ability to relate our receiver's performance to the underlying quantum dynamics also alludes to the potential for Rydberg atomic sensors to extend communication into the quantum regime. Current work in this area is ongoing [34–39]; we hope that our results further inspire quantum communication tools based on Rydberg vapor-cell platforms.

The authors would like to thank Michael Foss-Feig, Zachary Castillo, David Anderson, Elizabeth Goldschmidt, and Joe Britton for helpful discussions and comments. This work is supported by the Quantum Science and Engineering Program of the Office of the Secretary of Defense.

[1] W. L. Stutzman and G. A. Thiele, *Antenna Theory and Design*, 3rd ed. (Wiley, Hoboken, NJ, 2012).
[2] J. L. Volakis, *Antenna Engineering Handbook*, 4th ed. (McGraw-Hill Education, New York, 2007).
[3] L. J. Chu, Physical limitations of omni-directional antennas, J. Appl. Phys. **19**, 1163 (1948).
[4] H. A. Wheeler, Fundamental limitations of small antennas, Proc. IRE **35**, 1479 (1947).
[5] R. F. Harrington, Effect of antenna size on gain, bandwidth, and efficiency, J. Res. Natl. Bur. Stand. **64**, 1 (1960).
[6] J. S. McLean, A re-examination of the fundamental limits on the radiation Q of electrically small antennas, IEEE Trans, Antennas Propag. **44**, 672 (1996).
[7] C. Pfeiffer, Fundamental efficiency limits for small metallic antennas, IEEE Trans. Antennas Propag. **65**, 1642 (2017).
[8] S. R. Best, Electrically small resonant planar antennas: Optimizing the quality factor and bandwidth, IEEE Antennas Propag. Mag. **57**, 38 (2015).
[9] T. Nan *et al.*, Acoustically actuated ultra-compact NEMS magnetoelectric antennas, Nat. Commun. **8**, 296 (2017).
[10] S. E. Sussman-Fort and R. M. Rudish, Non-Foster impedance matching of electrically-small antennas, IEEE Trans. Antennas Propag. **57**, 2230 (2009).
[11] In realistic quantum sensors, one must always evaluate experimental losses in signal-to-noise ratio, such as quantum inefficiencies and technical noise, to quantitatively explain observed quantum fluctuations. Such imperfections can often be absorbed into new effective parameters for which one operates at the SQL.
[12] S. A. Miller, D. A. Anderson, and G. Raithel, Radio-frequency-modulated Rydberg states in a vapor cell, New J. Phys. **18**, 053017 (2016).
[13] A. K. Mohapatra, M. G. Bason, B. Butscher, K. J. Weatherill, and C. S. Adams, A giant electro-optic effect using polarizable dark states, Nat. Phys. **4**, 890 (2008).
[14] S. Kumar, H. Fan, H. Kübler, A. J. Jahangiri, and J. P. Shaffer, Rydberg-atom based radio-frequency electrometry using frequency modulation spectroscopy in room temperature vapor cells, Opt. Express **25**, 8625 (2017).
[15] C. L. Holloway, M. T. Simons, J. A. Gordon, P. F. Wilson, C. M. Cooke, D. A. Anderson, and G. Raithel, Atom-based RF electric field Metrology: From self-calibrated measurements to subwavelength and near-field imaging, IEEE Transactions on Electromagnetic Compatibility **59**, 717 (2017).
[16] C. G. Wade, N. Šibalić, N. R. de Melo, J. M. Kondo, C. S. Adams, and K. J. Weatherill, Real-time near-field terahertz imaging with atomic optical fluorescence, Nat. Photonics **11**, 40 (2017).
[17] J. A. Sedlacek, A. Schwettmann, H. Kübler, R. Löw, T. Pfau, and J. P. Shaffer, Microwave electrometry with Rydberg atoms in a vapour cell using bright atomic resonances, Nat. Phys. **8**, 819 (2012).
[18] D. A. Anderson, E. G. Paradis, and G. Raithel, A hybrid polarization-selective atomic sensor for radio-frequency field detection with a passive resonant-cavity field amplifier, Appl. Phys. Lett. **113**, 073501 (2018).
[19] D. A. Anderson, E. Paradis, G. Raithel, R. E. Sapiro, and C. L. Holloway, High-resolution antenna near-field imaging and sub-THz measurements with a small atomic vapor-cell sensing element, arXiv:1804.09789.
[20] D. H. Meyer, K. C. Cox, F. K. Fatemi, and P. D. Kunz, Digital communication with Rydberg atoms and amplitude-modulated microwave fields, Appl. Phys. Lett. **112**, 211108 (2018).
[21] A. B. Deb and N. Kjærgaard, Radio-over-fiber using an optical antenna based on Rydberg states of atoms, Appl. Phys. Lett. **112**, 211106 (2018).
[22] Y. Jiao, X. Han, J. Fan, G. Raithel, J. Zhao, and S. Jia, Atom-based quantum receiver for amplitude- and frequency-modulated baseband signals in high-frequency radio communication, arXiv:1804.07044.
[23] V. Gerginov, F. C. S. da Silva, and D. Howe, Prospects for magnetic field communications and location using quantum sensors, Rev. Sci. Instrum. **88**, 125005 (2017).
[24] C. Sayrin, I. Dotsenko, X. Zhou, B. Peaudecerf, T. Rybarczyk, S. Gleyzes, P. Rouchon, M. Mirrahimi, H. Amini, M. Brune, J.-M. Raimond, and S. Haroche, Real-time quantum feedback prepares and stabilizes photon number states, Nature (London) **477**, 73 (2011).
[25] C. E. Shannon, Communication in the presence of noise, Proc. IRE **37**, 10 (1949).
[26] T. Gallagher, *Rydberg Atoms*, 1st ed., Cambridge Monographs on Atomic, Molecular and Chemical Physics No. 3 (Cambridge University Press, Cambridge, England, 2005).
[27] Statistical error bars representing 1 standard deviation are shown for all data where the error bar is larger than the displayed point.
[28] Traditional AM radio receiver antennas in cars (meter scale) are a good example, which operate with approximately 5% efficiency to reach audio bandwidths [1].
[29] N. Zhu and R. W. Ziolkowski, Broad-bandwidth, electrically small antenna augmented with an internal non-Foster element, IEEE Antennas Wireless Propag. Lett. **11**, 1580 (2012).
[30] N. Šibalić, J. D. Pritchard, C. S. Adams, and K. J. Weatherill, ARC: An open-source library for calculating properties of alkali Rydberg atoms, Comput. Phys. Commun. **220**, 319 (2017).
[31] M. G. Bason, M. Tanasittikosol, A. Sargsyan, A. K. Mohapatra, D. Sarkisyan, R. M. Potvliege, and C. S. Adams, Enhanced electric field sensitivity of rf-dressed Rydberg dark states, New J. Phys. **12**, 065015 (2010).

[32] For communication purposes, absolute determination of the electric field strength is not necessary. When necessary, signal recovery techniques can be used as real-time calibrations.

[33] C. L. Degen, F. Reinhard, and P. Cappellaro, Quantum sensing, Rev. Mod. Phys. **89**, 035002 (2017).

[34] J. Han, T. Vogt, C. Gross, D. Jaksch, M. Kiffner, and W. Li, Coherent Microwave-to-Optical Conversion via Six-Wave Mixing in Rydberg Atoms, Phys. Rev. Lett. **120**, 093201 (2018).

[35] B. T. Gard, K. Jacobs, R. McDermott, and M. Saffman, Microwave-to-optical frequency conversion using a cesium atom coupled to a superconducting resonator, Phys. Rev. A **96**, 013833 (2017).

[36] H. Hattermann, D. Bothner, L. Y. Ley, B. Ferdinand, D. Wiedmaier, L. Sárkány, R. Kleiner, D. Koelle, and J. Fortágh, Coupling ultracold atoms to a superconducting coplanar waveguide resonator, Nat. Commun. **8**, 2254 (2017).

[37] W. Chen, K. M. Beck, R. Bücker, M. Gullans, M. D. Lukin, H. Tanji-Suzuki, and V. Vuletić, All-optical switch and transistor gated by one stored photon, Science **341**, 768 (2013).

[38] Y.-Y. Jau, A. M. Hankin, T. Keating, I. H. Deutsch, and G. W. Biedermann, Entangling atomic spins with a Rydberg-dressed spin-flip blockade, Nat. Phys. **12**, 71 (2016).

[39] L. Li and A. Kuzmich, Quantum memory with strong and controllable Rydberg-level interactions, Nat. Commun. **7**, 13618 (2016).